



Published in final edited form as:

ACS Nano. 2015 February 24; 9(2): 1837–1847. doi:10.1021/nn506750r.

## Atherosclerotic Plaque Targeting Mechanism of Long-Circulating Nanoparticles Established by Multimodal Imaging

Mark E. Lobatto<sup>†,‡</sup>, Claudia Calcagno<sup>†</sup>, Antoine Millon<sup>†,§</sup>, Max L. Senders<sup>†</sup>, Francois Fay<sup>†</sup>, Philip M. Robson<sup>†</sup>, Sarayu Ramachandran<sup>†</sup>, Tina Binderup<sup>†,||</sup>, Maarten P.M. Paridaans<sup>†</sup>, Steven Sensarn<sup>⊥</sup>, Stephan Rogalla<sup>⊥</sup>, Ronald E. Gordon<sup>#</sup>, Luis Cardoso<sup>¶</sup>, Gert Storm<sup>^,^</sup>, Josbert M. Metselaar<sup>^</sup>, Christopher H. Contag<sup>⊥</sup>, Erik S. G. Stroes<sup>‡</sup>, Zahi A. Fayad<sup>†</sup>, and Willem J.M. Mulder<sup>\*,†,‡</sup>

<sup>†</sup>Translational and Molecular Imaging Institute, Department of Radiology, Icahn School of Medicine at Mount Sinai, One Gustave L. Levy Place, New York, New York 10029, United States  
<sup>‡</sup>Department of Vascular Medicine, Academic Medical Center, Amsterdam, Meibergdreef 9, 1105 AZ, The Netherlands  
<sup>§</sup>Department of Vascular Surgery, University Hospital of Lyon, 69000 Lyon, France  
<sup>||</sup>Department of Clinical Physiology, Nuclear Medicine & PET and Cluster for Molecular Imaging, Rigshospitalet & University of Copenhagen, 2200 Copenhagen, Denmark  
<sup>⊥</sup>Departments of Radiology, Pediatrics and the Molecular Imaging Program, Stanford University, Stanford, California 94305, United States  
<sup>#</sup>Department of Pathology, Mount Sinai Hospital, One Gustave L. Levy Place, New York, New York 10029, United States  
<sup>¶</sup>Department of Biomedical Engineering, The City College of New York, New York, New York 10031, United States  
<sup>^</sup>Department of Targeted Therapeutic, MIRA Institute, University of Twente, Enschede, 7500 AE, The Netherlands  
<sup>^</sup>Utrecht Institute for Pharmaceutical Sciences, Utrecht University, Utrecht 3512 JE, The Netherlands

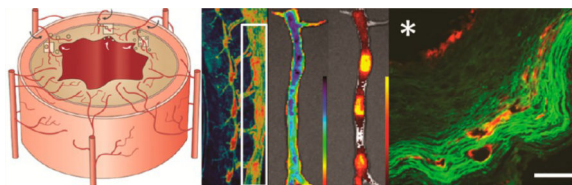
### Abstract

Atherosclerosis is a major cause of global morbidity and mortality that could benefit from novel targeted therapeutics. Recent studies have shown efficient and local drug delivery with nanoparticles, although the nanoparticle targeting mechanism for atherosclerosis has not yet been fully elucidated. Here we used *in vivo* and *ex vivo* multimodal imaging to examine permeability of the vessel wall and atherosclerotic plaque accumulation of fluorescently labeled liposomal nanoparticles in a rabbit model. We found a strong correlation between permeability as established by *in vivo* dynamic contrast enhanced magnetic resonance imaging and nanoparticle plaque accumulation with subsequent nanoparticle distribution throughout the vessel wall. These key observations will enable the development of nanotherapeutic strategies for atherosclerosis.

\*Address correspondence to willem.mulder@mssm.edu.

*Conflict of Interest:* The authors declare no competing financial interest.

*Supporting Information Available:* Graphs of imaging parameters, optical imaging of en face prepared aortas, correlation map between DCE-MRI and EB NIRF, overview of abdominal aortas that were injected with EB and Cy7-LN, overview control aortas. Movies of dualaxis confocal microscopy and fiber-scope. This material is available free of charge via the Internet at <http://pubs.acs.org>.



## Keywords

nanoparticle; DCE-MRI; atherosclerosis; nanomedicine; targeting; imaging; *in vivo* microscopy

Cardiovascular disease is the leading cause of death in the world.<sup>1</sup> The most manifest contributor to cardiovascular morbidity and mortality is atherosclerosis, a systemic disease affecting arteries, which can cause clinical complications such as myocardial infarction and stroke when atherosclerotic plaques rupture.<sup>2</sup> Atherosclerosis itself is recognized as a chronic inflammatory disease with accumulation of lipids and immune cells in the arterial wall.<sup>3</sup> As an alternative to lipid-lowering drugs such as statins, immunomodulatory treatments are currently under investigation in multiple clinical trials, as they have the potential to diminish the inflammatory component of atherosclerosis, a fundamental trigger of plaque rupture.<sup>4</sup> A serious drawback of immunomodulatory drugs, however, is the prospect of systemic immunosuppression and other off-target effects. A method to circumvent marked side effects is by their encapsulation in, or attachment to, nanoparticles.<sup>5,6</sup> Besides limiting side effects, nanoparticles are also known for enhancing therapeutic efficacy by increasing drug concentrations in diseased tissues.<sup>7</sup> It has been acknowledged that nanoparticles and macromolecules accumulate in certain types of malignancies and at sites of inflammation due to enhanced vascular permeability.<sup>8</sup> While normal endothelium will not permit the extravasation of nanoparticles due to tight endothelial junctions, gaps in endothelial junctions at sites of disturbed shear stress facilitate paracellular extravasation of macromolecules and nanoparticles.<sup>9</sup>

We have previously shown that long-circulating nanoparticles loaded with an anti-inflammatory drug accumulate within atherosclerotic lesions and induce local anti-inflammatory effects.<sup>10</sup> However, the nanoparticle targeting mechanism in this disease has not been elucidated.<sup>11</sup> The vessel wall of medium- and large-sized arteries is supplied with nutrients and oxygen through a microvessel network named the vasa vasorum (Figure 1). Similar to hypoxia-induced angiogenesis in tumors, this microvessel network surrounding arteries expands through angiogenesis and the formation of new blood vessels as a result of hypoxia within atherosclerotic lesions.<sup>12</sup> These newly formed vessels are poorly structured and inadequately delineated by endothelial cells, which favors the extravasation of inflammatory cells and lipids and contributes to further plaque buildup.<sup>13</sup> Nanoparticles may accumulate at such sites of dysfunctional and disrupted endothelium in the same fashion, which is schematically depicted in Figure 1. In the current study, we set out to thoroughly investigate nonspecific plaque targeting of long-circulating nanoparticles with a variety of *in vivo* and *ex vivo* imaging methods.

## RESULTS AND DISCUSSION

### *In Vivo* Imaging of Healthy and Atherosclerotic Rabbits

We initially investigated differences in overall vessel wall morphology, permeability, and vasa vasorum in New Zealand white male rabbits fed a chow diet versus rabbits with atherosclerotic lesions in the abdominal aorta induced by both a high-cholesterol diet and balloon angioplasties. First, we performed *in vivo* magnetic resonance imaging (MRI) on a clinical 3 T scanner to examine the mean vessel wall area (Figure 2a), showing a thickened arterial wall in the atherosclerotic rabbit, which was quantified on  $T_2$ -weighted ( $T_2W$ ) images ( $P < 0.0001$ , overview of all parameters can be found in Table 1 and Supplementary Figure 1).

Dynamic contrast enhanced (DCE)-MRI is an *in vivo* imaging technique that allows quantification of vascular permeability noninvasively, by dynamically acquiring  $T_1$ -weighted ( $T_1W$ ) MR images before and continuously during and after injection of a gadolinium-based contrast agent over a certain time frame. These data can be used to examine the kinetics of contrast agent accumulation within a tissue of interest.<sup>15</sup> This technique has matured in the field of oncology but has only recently been modified to measure vascular permeability of atherosclerotic plaques.<sup>16</sup> For imaging of atherosclerosis, black-blood MRI is a useful technique to suppress blood flow and signal from the contrast agent in the arterial lumen in order to clearly differentiate the arterial wall from blood flow.<sup>17</sup> A black-blood DCE-MRI technique has previously been shown to correlate with the amount of neovessels in atherosclerosis when imaging a single 3 mm thick axial slice in a single vascular bed.<sup>18</sup> Because of the predominantly heterogeneous nature of atherosclerosis, with large lipid deposits, inflammatory cells, and endothelial disruption in multiple vascular beds with dissimilar distribution in multiple areas' and even within the same model, single or multiple 3 mm thick slices will not give an accurate depiction of the overall permeability of a vascular region of interest. We consequently developed a black-blood 3D DCE-MRI technique, which has the capacity to quantify permeability over a large vascular region, that is, the entire infra-renal abdominal aorta of a rabbit.<sup>19</sup> From this sequence, area under the contrast agent concentration time curves (IAUC) can be calculated, which provide a quantitative measure for the amount of contrast agent (Gd-DTPA, Magnevist) permeating through the vessel wall over a certain time period. Sagittal DCE images and reconstructed coronal IAUC maps are depicted for the aortas of healthy and atherosclerotic rabbits in Figure 2b, where a marked difference in IAUC within the abdominal aorta can be seen for healthy and atherosclerotic rabbits. The chow-fed rabbits had a homogeneous vessel wall with minute uptake of contrast agent, while the abdominal aortas of atherosclerotic rabbits were abundant with regions of permeability in a heterogeneous fashion. We quantified the IAUC 2 min after Gd-DTPA injection from 154 (12 contiguous regions of interest (ROI) drawn on the abdominal aorta on reformatted axial slices, giving a quantitated measure ( $P < 0.0001$ ).

After DCE-MRI acquisition was completed, conventional gadolinium contrast enhancement scans were also acquired. These scans can provide information on morphological plaque features,<sup>20</sup> though they cannot specify dynamic permeability of the plaque or vessel wall. As

expected, widespread signal enhancement can be seen throughout the entire abdominal aorta in atherosclerotic rabbits, compared to minimal signal enhancement in the chow-fed rabbits (Figure 2c,  $P = 0.0005$ ).

### Ex Vivo Imaging Methods

Next, we sacrificed a different set of animals ( $n = 1$  healthy,  $n = 2$  atherosclerosis) to demonstrate the disparity in extent of vasa vasorum and neovessels between the abdominal aortas of healthy and atherosclerotic rabbits. After euthanasia, a cut was made in the right atrium and the rabbit was perfused with heparinized saline from the left ventricle to clear the vasculature of blood. A lead-based polymer (Microfil MV-122) was then injected into the left ventricle under continuous pressure. The hardening of this polymer generates a mold of the vasculature and allows the isolation of the aorta and the vasa vasorum. Because the lead-based polymer is a potent computed tomography (CT) contrast agent, it is possible to visualize the arterial lumen and the surrounding vasa vasorum supplying the arterial wall. We used the micro-CT ( $\mu$ CT) imaging data to render three-dimensional images of the abdominal aortas by reconstructing continuous 6  $\mu$ m thick slices over a prolonged segment (Figure 2d), clearly exposing the difference in vasa vasorum burden in the atherosclerotic rabbits compared to the healthy rabbit. A single 6  $\mu$ m thick slice shows the difference in plaque thickness between the two aortas, as well as the irregularity of the lumen, and the extent of vasa vasorum.

To further investigate vascular permeability within the aortic wall and corroborate *in vivo* findings *ex vivo*, we intravenously injected the dye Evans Blue (EB) in both chow-fed and atherosclerotic rabbits. EB binds to albumin and stains sites with enhanced endothelial permeability. EB is most commonly used to detect a breakdown of the blood-brain barrier but can also be used to detect enhanced permeability in atherosclerosis.<sup>21</sup> A clear difference between the EB-stained surface areas of en face prepared thoracic aortas of rabbits fed a chow diet *versus* thoracic aortas of atherosclerotic rabbits was observed (Figure 2e,  $P = 0.033$ ). Due to intrinsic fluorescent properties, EB can also be visualized with fluorescence imaging, where in this instance we used an IVIS optical imaging system to measure differences between healthy and atherosclerotic abdominal aortas (Figure 2f,  $P = 0.02$ ).

To visualize the intima and plaque areas, en face sections of healthy and atherosclerotic abdominal aortas were harvested and consequently stained with 0.05% methylene blue and 100  $\mu$ M indocyanine green and then washed and subsequently imaged on a custom-built dual-axis confocal microscope.<sup>22–24</sup> The dual-axis confocal microscope design enables miniaturization with the potential of *in vivo* clinical imaging.<sup>25–27</sup> Individual frames of Supporting Information movies S1 and S2 are shown in Figure 2g, where a regularly structured endothelial lining can be seen in the healthy abdominal aorta and a cross section of plaque structure of the atherosclerotic abdominal aorta can be found.

Representative histological images of a healthy *versus* an atherosclerotic rabbit revealed a marked difference in vessel wall thickness with conventional hematoxylin and eosin staining, as well as the amount of vasa vasorum microvessels that were appreciated in the adventitia (the outermost connective tissue of the vessel) and within the plaque of atherosclerotic rabbits stained with the endothelial cell marker CD-31 (Figure 2h).

Lastly, transmission electron microscopy (TEM) images of a healthy vessel wall revealed continuous endothelial cells connected with tight junctions covering the luminal side of the vessel. In contrast, the atherosclerotic vessel wall revealed large paracellular gaps on the luminal side of the vessel wall, as well as a neovessel inside the cholesterol-filled plaque, of which examples are shown in Figure 2i.

### Nanoparticle Targeting in Atherosclerosis Is Reliant on Vascular Permeability

After obtaining a general overview of the distinct difference between aortas of healthy and atherosclerotic rabbits, we set out to measure the accumulation of nanoparticles in atherosclerotic lesions over time. All animals were first imaged with 3D DCE-MRI to assess vascular permeability of the abdominal aortas *in vivo*, after which the animals were intravenously injected with long-circulating liposomal nanoparticles. These nanoparticles were prepared by standard lipid film hydration methods followed by sonication<sup>28</sup> and were labeled with the near-infrared fluorophore Cy7. These Cy7-labeled liposomal nanoparticles (Cy7-LN) were allowed to circulate for different lengths of time (0.5, 6, and 24 h), and animals were subsequently sacrificed. Additionally, as before, animals were injected with EB 30 min prior to sacrifice. The abdominal aortas were harvested and consequently imaged with NIRF imaging. Since Cy7-LN and EB have distinctly different emission and excitation profiles, we were able to simultaneously image and consequently quantify (micro) vessel permeability as well as nanoparticle uptake (Supplementary Figure 2).

DCE-MRI IAUC was then quantified as mentioned above and paired with the fluorescent radiant efficiency of Cy7-LN in order to calculate the linear regression, after dividing the aorta in seven different regions. The identical ROIs that were used for Cy7-LN quantification were superimposed on the EB images and consequently used to model the linear regression, as well. Representative images of 3D DCE-MRI and NIRF images of abdominal aortas from rabbits in which Cy7-LN was allowed to circulate for a 30 min are shown in Figure 3a. There was a strong, positive correlation between Cy7-LN and IAUC ( $r^2 = 0.58$ ,  $P = 0.003$ ) after 30 min, similar to the correlation between Cy7-LN and EB ( $r^2 = 0.8$ ,  $P < 0.0001$ ) at that time point. The 6 h time point is presented in Figure 3b, where the abdominal aorta imaged with 3D DCE-MRI had several distinct regions of permeability, which visually corresponds to nanoparticle and EB extravasation in the exact same regions. Interestingly, the correlation gradually decreased after 6 h compared to the half hour time point for both DCE-MRI ( $r^2 = 0.56$ ,  $P = 0.002$ ) and EB ( $r^2 = 0.47$ ,  $P = 0.007$ ) and remained significant. After 24 h, there still was a visual semblance of Cy7-LN and permeability measured by MRI and NIRF, though the correlation between IAUC or EB and Cy7-LN was not significant for either ( $r^2 = 0.034$ ,  $P = 0.53$ ;  $r^2 = 0.08$ ,  $P = 0.33$ , respectively), which might indicate that nanoparticles initially accumulate at sites of enhanced permeability and subsequently disperse throughout the plaque. There was a positive correlation between IAUC and EB, as well,  $r^2 = 0.17$ ,  $P = 0.008$ , indicating that IAUC can serve as an *in vivo* marker for permeability (Supplementary Figure 3). In Supplementary Figure 4, an overview of all abdominal aortas injected at different time points is shown. As a control experiment, healthy rabbits were injected with Cy7-LN, as well, sacrificed at different time points, and imaged with NIRF. These images revealed no nanoparticle uptake (Supplementary Figure 5).

## Nanoparticles Disperse Throughout the Plaque over Time

Figure 1 indicates that nanoparticles can enter the plaque from the luminal side due to a dysfunctional endothelium or from microvessels present in the adventitia that originate from the vasa vasorum. To further validate how the nanoparticles enter the plaque from the lumen, we first investigated intact aortas with intravascular imaging using a fluorescence fiberscope at the same time points as above (0.5, 6, and 24 h). This device was developed from the Spyglass (Boston Scientific, Boston, MA) fiberscope, which we converted from a white light device to a wide-field fluorescence fiberscope—this device has a 1 mm outer diameter and is used clinically as a white light system. It was designed as a finder scope to look at superficial fluorescent signals and to guide the placement of the miniaturized dual-axis microscope. To comply with the current filter set of the device, we synthesized and injected liposomal nanoparticles that were labeled with LI-800CW, a fluorophore with an emission wavelength peak of 785 nm. After sacrificing the animals, the whole aorta was harvested and a fiberscope was inserted in the aortic arch and advanced down to the iliac bifurcation. The scope was consequently retracted to detect signal from the aortic lumen. Signal of LI-800CW-labeled liposomal nanoparticles was detected throughout the abdominal atherosclerotic aortas (representative images in Supporting Information movie S3). Representative fluorescence images with their corresponding white light images and a pixel intensity map are presented in Figure 4a–c. Bright fluorescence was observed for the atherosclerotic animals injected with nanoparticles, indicative of luminal nanoparticle plaque entering, where minimal fluorescent signal was picked up in the control aortas.

To corroborate the above data and to study nanoparticle targeting through the neovessels from the adventitial side, we additionally injected Cy5.5-labeled liposomal nanoparticles (Cy5.5-LN) in three atherosclerotic rabbits and allowed these to circulate the same varying durations in order to perform fluorescence microscopy on axial aortic sections. Figure 5a shows a reconstructed fluorescence microscopy image of 30–40 adjacent images acquired at a 20× magnification of a 5 μm thick section of the aorta of the rabbit sacrificed at 30 min, with an individual 20× image next to it. At this time point, the nanoparticles were found to be confined to microvessels in the adventitia, while in Figure 5b, at the 6 h time point, it can be seen that Cy5.5-LN started to extravasate from these microvessels and to enter from the luminal side, corroborating our endoscopy findings. After 24 h (Figure 5c), the nanoparticles were seen both at the luminal side and at the vasa vasorum but also diffused throughout the plaque, giving a plausible explanation for the temporal decrease in correlation when comparing LN extravasation with both *in vivo* and *ex vivo* permeability measurements.

An alternative theory for nanoparticle accumulation at inflammatory sites is that nanoparticles are taken up by mononuclear cells in the circulation or in the spleen and consequently migrate to sites of enhanced permeability such as brain ischemia and myocardial infarction.<sup>29</sup> To this end, we withdrew whole blood from the Cy7-LN-infused animals, as well, and centrifuged it over a histopaque gradient, which separates whole blood into separate layers of cells (*i.e.*, red blood cells, serum, and mononuclear cells). Since we did not see significant association of the fluorescent label Cy7 with mononuclear cells in this instance (Supplementary Figure 7), we deem this nanoparticle targeting mechanism less likely as a possible explanation for the pronounced accumulation of nanoparticles into



plaques, although it might contribute, even though the targeting would still rely on endothelial permeability. Similar to other studies with longcirculating nanoparticles, uptake in the mononuclear phagocyte system organs such as the liver, spleen, and bone marrow were observed, which needs to be taken into consideration when using nanoparticles to deliver drugs to atherosclerotic plaques.

A better understanding of nanoparticle targeting principles in atherosclerotic disease is mandatory for the aimed development of nanoparticle therapeutics. Here, we first showed the general differences of vessel wall morphology, permeability, and vasa vasorum in chow-fed rabbits and rabbits with atherosclerotic lesions with a vast variety of imaging methods. More importantly, and the aim of the current study, we consequently used both *in vivo* and *ex vivo* imaging methods to demonstrate that nanoparticles extravasate at sites of dysfunctional and disrupted endothelium in advanced atherosclerotic lesions in a rabbit atherosclerosis model. These findings are of interest for two essential reasons. First, long-circulating liposomal nanoparticles extravasate at atherosclerotic lesions with enhanced permeability and can therefore be employed for drug delivery purposes. Second, the technique 3D DCE-MRI can be used as a method to interrogate vascular permeability over a large vascular bed, consequently giving indication if a specific atherosclerotic lesion might be amenable to nanoparticle therapy.

It is crucial to take into consideration the differences in vessel wall dimensions between different atherosclerosis models. Although in mouse lesions the presence of VEGF-induced neovessels has been reported,<sup>30</sup> this only occurs at very advanced stages, in large plaques in which hypoxia becomes relevant.<sup>31</sup> This implies that accumulation of PEG-coated long-circulating nanoparticles is abundant only in plaques with an angiogenically activated vasa vasorum, which is the case in the rabbit model. In previous studies, we have shown efficient plaque accumulation in mice with high density lipoprotein nanoparticles, due to the material's natural targeting properties, unrelated to plaque neovascularization.<sup>11,32</sup>

Although the aforementioned nonspecific targeting occurs in larger neovessel-rich plaques, our data with long-circulating liposomal nanoparticles are extrapolatable to long-circulating PEG-functionalized nanoparticles with similar dimensions, such as PLGA-PEG-based and other PEG-coated polymeric nanoparticles,<sup>33</sup> as well as nanoemulsions.<sup>34</sup>

The unique combination of novel imaging techniques, the animal model, and nanoparticle labeling facilitated the present study. The approach could potentially also be used to evaluate active targeting with nanoparticles that are functionalized with targeting ligands to specific cells within the plaque as the overall vascular permeability will facilitate the accumulation of nanoparticles in the plaque.<sup>35</sup>

A further evaluation in regards to, for instance, optimum nanoparticle size for atherosclerotic plaque permeation, similar to studies performed in cancer, would be of benefit to extrapolate these findings for smaller or larger nanoparticles,<sup>36</sup> as well as investigating other nanoparticle shapes opposed to the spherical nanoparticles used in this study.<sup>37</sup>

## CONCLUSIONS

Nanoparticle targeting in atherosclerosis is reliant on endothelial permeability of the vessel wall and vasa vasorum. Additionally, 3D DCE-MRI can be used as a predictor for nanoparticle accumulation in advanced atherosclerotic lesions in preclinical models.

## MATERIALS AND METHODS

### Liposomal nanoparticle Preparation

Long-circulating liposomal nanoparticles were prepared as follows: 400  $\mu\text{mol}$  of phospholipids: 61.5% of 1,2-dipalmitoyl-*sn*-glycero-3-phosphocholine (DPPC), 33.3% of cholesterol, 5.0% of 1,2-distearoyl-*sn*-glycero-3-phosphoethanolamine-*N*-[methoxy(polyethylene glycol)-2000] (PEG-DSPE), and 0.2% of DSPE-Cy5.5 or DSPE-Cy7 were dissolved in 5 mL of a chloroform/methanol (4:1 v/v) solution (phospholipids were purchased from Avanti Polar Lipids, and Cy5.5 and Cy7 were obtained from Keracast Inc.). The phospholipid solution was transferred into a round-bottom flask. A thin lipid film was then created by removing the solvents using a rotary evaporator and subsequently dried with a stream of nitrogen for 1 h. The thin lipid film was hydrated with 10 mL of warm (70 °C) phosphate buffer saline (PBS) and mixed using glass beads to form liposomes. The solution was homogenized on ice for 30 min using an ultrasonic homogenizer (Biologics, USA). After homogenization, large insoluble aggregates were removed by centrifugation at 500g for 5 min. Finally, the solution was sterile filtered through a 0.2  $\mu\text{m}$  pore size membrane inside a biological safety cabinet. The effective diameter, polydispersity index, and zeta-potential of the liposomal nanoparticles was 123 nm ( $\pm 2.5$ ), 0.120 ( $\pm 0.01$ ), and  $-14.4$  mV ( $\pm 2.5$ ), respectively. Rabbits were injected with liposomal nanoparticles according to fluorescent dye per body weight (0.5  $\mu\text{mol}$  dye/kg).

### Animal Model and Preparation

Twenty-one male New Zealand white rabbits were included in this study. Advanced atherosclerosis was induced in 16 of 21 rabbits by a well-established method,<sup>28</sup> consisting of a combination of a high cholesterol diet (0.3% for 2 months, 0.15% for 4 months, Research Diets Inc.) and double balloon injuries of the thoracic and abdominal aortas. The remaining 5 rabbits were fed a standard chow diet and used as healthy controls. Balloon injury was performed by introducing a 4F-Fogarty embolectomy catheter (Edwards Life-Sciences) through a surgically exposed femoral artery, advancement of the embolectomy balloon into the thoracic aorta, inflation of the balloon to 2 atm, and three continuous pullbacks to the iliac bifurcation under fluoroscopic guidance, while decreasing pressure to avoid the creation of aneurysms. The femoral artery was subsequently ligated, and balloon injury was repeated from the contralateral extremity 4 weeks later. Surgeries were performed under anesthesia with intramuscular Ketamine (35 mg/kg) and Xylazine (5 mg/kg). Intravenous injections of Gd-DTPA, nanoparticles, and EB were administered through a 22 gauge catheter placed in the marginal ear vein. Animals were sacrificed with an intravenous overdose of sodium pentobarbital; a cut in the right atrium was made, and animals were perfused with heparinized saline through the left ventricle to clear the vasculature of blood.



All animal experiments were approved by the Institutional Animal Care and Use Committee at the Icahn School of Medicine at Mount Sinai.

### MRI Acquisition

Animals were imaged using a 3 T whole-body scanner (Philips Achieva) using a product 8 channel knee coil. Imaging was performed approximately 6 months after diet initiation. After scout scans and time-of-flight noncontrast enhanced angiography to localize the abdominal aorta, a 2D multislice black-blood sequence was used to quantify atherosclerotic burden from the left renal artery to the iliac bifurcation. Imaging parameters were: repetition time (TR), 2000 ms; echo time (TE), 40 ms; flip angle, 90°; refocusing flip angle, 120°, echo train length (ETL), 5; slice thickness, 3 mm; interslice gap, 4.5 mm; in-plane spatial resolution, 0.5 mm<sup>2</sup>; field of view (FOV), 120 mm<sup>2</sup>; 1 signal average; 23 slices; orientation, axial. Black-blood was obtained using a double inversion recovery technique. A 3D turbo field echo sequence with motion-sensitized driven equilibrium preparation for black-blood imaging was used to quantify the uptake of a gadolinium-based contrast agent (gadopentetate dimeglumine, Magnevist, Bayer Healthcare) from the right renal artery to the iliac bifurcation. Imaging parameters were as follows: TR, 6.2 ms; TE, 2.8 ms; flip angle, 20°; ETL, 80; spatial resolution, 0.6 mm<sup>3</sup>; FOV, 160 mm<sup>2</sup>; 20 slices; orientation, sagittal. This sequence was used before and 10 min after contrast agent injection to quantify contrast agent accumulation in the vessel wall (acquisition with 6 signal averages). Before and during contrast agent injection, the same sequence was used with 3 signal averages (time resolution 32 s) to perform 3D DCE-MRI.

### Imaging Data Analysis

Three-dimensional DCE-MRI data were analyzed by manually drawing ROIs in axially reformatted images in OsiriX (Pixmeo) on the outer and inner vessel wall on contiguous slices from the left renal artery to the iliac bifurcation. From here, the IAUC were calculated with a custom-made program written in Matlab (<http://www.mathworks.com/>). The IAUC after 2 min was used as a time point for data analysis. IAUC was calculated on a pixel-by-pixel basis. MR signal intensity over time was normalized to vertebral muscle signal intensity before the injection of contrast agent. Inner and outer vessel wall contours were superimposed to IAUC parametric maps to calculate the average IAUC in the vessel wall for each traced axial slice. The aortas were divided into 6 or 7 different regions according to the length of the aorta. The total IAUC of each region was divided from the total IAUC of the whole abdominal aorta.

### Evans Blue Experiments

Thirty minutes prior to sacrifice of the animals, 0.5% of 6 mL of Evans Blue (Sigma-Aldrich, St. Louis, MO) in 1 × PBS was administered through a 22 gauge catheter in the marginal ear vein.<sup>38</sup> Photographs of the en face prepared thoracic aortas were taken with a Canon S500 digital camera.

### Near-Infrared Fluorescence Imaging

Whole blood was withdrawn prior to euthanization, of which 4 mL was spun down over histopaque density gradients 1083 and 1119 (Sigma-Aldrich) according to a protocol previously described to separate mononuclear cells and serum.<sup>29</sup> After euthanization, the thoracic and abdominal aortas were harvested, measured in length, and imaged with a Xenogen IVIS-200 optical imaging system. The excitation and emission filter for Evans Blue was set to 605 and 680 nm with an exposure time of 10 s, binning at 4, FOV = 22.8 cm. The filters for Cy7 excitation and emission were set to 745 and 800 nm. NIRF imaging data were analyzed by placing ROIs of 1 cm height on the excised abdominal aortas starting at the left renal artery, continuing to the iliac bifurcation, resulting in 6 or 7 ROIs per aorta. The aortas were first placed on the EB data and were later superimposed for the Cy7 wavelength. The total radiance efficiency [ $\text{p/s}/[\mu\text{W}/\text{cm}^2]$ ] was used for data analysis. The total radiance efficiency of each region was divided from the total radiance efficiency of the whole abdominal aorta.

### $\mu$ CT Imaging

In a subset of rabbits (1 healthy and 2 atherosclerotic rabbits), after euthanasia and perfusion with heparinized saline, MV-122 (Flow Tech Inc., MA) was injected into the left ventricle under continuous pressure. After a 30 min waiting period and hardening of the polymer, the abdominal aortas were harvested and stored in 4% paraformaldehyde. The following day, aortas were scanned using a  $\mu$ CT scanner (1172 SkyScan, Belgium) with an isotropic voxel size of  $6\ \mu\text{m} \times 6\ \mu\text{m}$  (60 kV, 167  $\mu\text{A}$ , 147 ms exposure time per projection, 10 megapixel camera, 12 mm FOV, 512 consecutive projections per scan). To produce high-contrast, low-noise images, the projections were averaged five times, and a median filter was used to prevent speckle noise formation. Seven vertically connected scans were performed to cover the entire length of each aorta. Approximately 7000 images per sample were reconstructed from X-ray projections using the back-projection reconstruction algorithm in NRecon software (Skyscan, V1.6.1.1, SkyScan). Hounsfield unit calibration of images was performed in CTAn software (CT Analyzer, v.1.6.1, SkyScan, Belgium). After image density calibration, the separation (image segmentation) between microfil, lumen, and soft tissues in each scan was performed using a mean global thresholding procedure. The threshold value was determined by analyzing the images using an edge detection algorithm (ImageJ v 1.37, National Institutes of Health).<sup>39,40</sup> The 3D rendering was performed with Mimics (V17.0, Materialise, MI).

### Dual-Axis Confocal Microscopy

This microscope performs rapid optical sectioning of tissues and produces a 3D volumetric data set in about 3 min. Each of the 10 samples was imaged twice (once per tissue side). Methylene blue and indocyanine green fluorescence signals were acquired simultaneously using the DAC microscope's two-color imaging capability [utilizing 660 (Coherent CUBE) and 785 nm (Melles Griot) lasers for excitation]. Due to relatively weaker signal levels in the methylene blue data,  $2 \times 2$  downsampling was used to improve signal-to-noise of each optical section in the 3D volumetric data set. Image processing was performed using open-source software (ImageMagick and AviSynth).

## Fiberscope

Intact aortas were imaged using a fluorescence endoscopy system based on the SpyGlass fiberscope (Boston Scientific). The fiberscope contains a central imaging bundle composed of 6600 multimode fibers fused together. These fibers relay a 70° field of view to cameras on the proximal detection apparatus (an Andor Luca S EMCCD camera for fluorescence detection and a Hitachi KP-D20B color camera for white-light imaging, selectable by a removable 45° mirror). The fiberscope also incorporates 225 peripheral illumination fibers which transmit either a white-light LED (for white-light imaging) or a 785 nm laser (for fluorescence imaging) to the sample (selectable *via* electronic switches). The fiberscope was delivered into the aorta using a 1.8 mm diameter plastic tube coupled to an aquarium air pump and pressure regulator to partially insufflate the aorta and improve visibility. Videos were recorded using Andor SOLIS software (for the EMCCD) and VideoHome Technology GrabBee (for the color camera, in conjunction with a StarTech SVID2USB2NS analog video capture cable). A combination of Matlab, ImageMagick, and Avi-Synth scripts were used to process the data and generate videos and still frames.

## Fluorescence Microscopy

After NIRF imaging, aortas were cut into 5 mm thick sections, embedded in OCT or paraffin blocks (for histology), and stored in -80 °C or at room temperature. OCT blocks were cut into 5 µm thick sections with a cryotome and were mounted on a microscope slide with Vectamount and sealed. Slides were imaged the following day on a Zeiss Axioplan 2 fluorescence microscope with a Cy5 filter. The autofluorescence of the elastic laminae of the vessel wall at the FITC wavelength was used as an anatomical guide.

## Histology

A selection of 5 mm aortic rings from the harvested abdominal aortas of control and atherosclerotic rabbits was placed in 4% paraformaldehyde. Twenty-four hours later, the rings were embedded in paraffin and cut into sections of 5 µm thickness. The sections were stained with conventional hematoxylin and eosin or CD-31 staining for endothelial cells (Dako) according to previous methods.<sup>18</sup> The sections were digitally imaged with a Nikon Eclipse E400 microscope, a Nikon DS-U1 camera box, and a Nikon DS-5 M camera.

## Transmission Electron Microscopy

Aortic rings of 2 mm of abdominal aortas of harvested healthy and atherosclerotic rabbits were cut below the celiac artery directly after sacrifice and consequently deposited in 3.0% glutaraldehyde in 0.2 M sodium cacodylate as a buffer in pH 7.4. The aortic tissue was subsequently washed in buffer and treated with osmium tetroxide 1% for 1 h. Afterward, the tissue was dehydrated in graded steps of ethanol, then cleared with propylene oxide, and embedded in EMbed 812 (Electron Microscopy Sciences). Ultrathin sections were cut and mounted on a grid for imaging. TEM image acquisition was performed with a Hitachi 7650 TEM operated at 80 kV coupled to a Scientific Instruments and Applications (SIA) digital camera controlled by Maxim CCD software.

## Statistical Analysis

Data are presented as mean  $\pm$  standard deviation. Unpaired student's t tests were used where appropriate. For the linear regression analysis of EB, Cy7-LN and DCE-MRI data, data were matched according to anatomical location. *P* values of  $<0.05$  were considered to be statistically significant. Prism 6 (Graphpad) was used for statistical analysis.

## Supplementary Material

Refer to Web version on PubMed Central for supplementary material.

## Acknowledgment

This work was supported by the National Heart, Lung, and Blood Institute, National Institutes of Health, as a Program of Excellence in Nanotechnology (PEN) Award, Contract No. HHSN268201000045C (Z.A.F.), NIH Grants R01 HL118440 (W.J.M.M.), R01 HL125703 (W.J.M.M.), R01 EB009638 (Z.A.F.), NWO Vidi 91713324 (W.J.M.M.), FP7 NANOATHERO, and the Dutch network for Nanotechnology NanoNextNL in the subprogram "Drug Delivery". M.E.L. was partially supported by the International Atherosclerosis Society and the foundation "De Drie Lichten" in The Netherlands.  $\mu$ CT was supported with NIH Grant DK103362, NSF Grants MRI-1229449 and CMMI-1333560 (L.C.). Fluorescence microscopy was performed at the MSSM-Microscopy Shared Resource Facility, supported with funding from NIH-NCI shared resources grant (5R24 CA095823-04), NSF Major Research Instrumentation grant (DBI-9724504), and NIH shared instrumentation grant (1 S10 RR0 9145-01).

## REFERENCES AND NOTES

1. Mitka M. New Basic Care Goals Seek To Rein in Global Rise in Cardiovascular Disease. *JAMA*. 2012; 308:1725–1726. [PubMed: 23117755]
2. Libby P. Inflammation in Atherosclerosis. *Nature*. 2002; 420:868–874. [PubMed: 12490960]
3. Ross R. Atherosclerosis—An Inflammatory Disease. *N. Engl. J. Med.* 1999; 340:115–126. [PubMed: 9887164]
4. Tabas I, Glass CK. Anti-inflammatory Therapy in Chronic Disease: Challenges and Opportunities. *Science*. 2013; 339:166–172. [PubMed: 23307734]
5. Mulder WJM, Jaffer FA, Fayad ZA, Nahrendorf M. Imaging and Nanomedicine in Inflammatory Atherosclerosis. *Sci. Transl. Med.* 2014; 6:239sr1. [PubMed: 24898749]
6. Wagner V, Dullaart A, Bock A-K, Zweck A. The Emerging Nanomedicine Landscape. *Nat. Biotechnol.* 2006; 24:1211–1217. [PubMed: 17033654]
7. Allen TM, Cullis PR. Drug Delivery Systems: Entering the Mainstream. *Science*. 2004; 303:1818–1822. [PubMed: 15031496]
8. Fang J, Nakamura H, Maeda H. The EPR Effect: Unique Features of Tumor Blood Vessels for Drug Delivery, Factors Involved, and Limitations and Augmentation of the Effect. *Adv. Drug Delivery Rev.* 2011; 63:136–151.
9. Tarbell JM. Shear Stress and the Endothelial Transport Barrier. *Cardiovasc. Res.* 2010; 87:320–330. [PubMed: 20543206]
10. Lobatto ME, Fayad ZA, Silvera S, Vucic E, Calcagno C, Mani V, Dickson SD, Nicolay K, Banciu M, Schifferers RM, et al. Multimodal Clinical Imaging to Longitudinally Assess a Nanomedical Anti-inflammatory Treatment in Experimental Atherosclerosis. *Mol. Pharmaceutics*. 2010; 7:2020–2029.
11. Lobatto ME, Fuster V, Fayad ZA, Mulder WJM. Perspectives and Opportunities for Nanomedicine in the Management of Atherosclerosis. *Nat. Rev. Drug Discovery*. 2011; 10:835–852.
12. Moreno PR, Purushothaman KR, Sirol M, Levy AP, Fuster V. Neovascularization in Human Atherosclerosis. *Circulation*. 2006; 113:2245–2252. [PubMed: 16684874]
13. Doyle B, Caplice N. Plaque Neovascularization and Antiangiogenic Therapy for Atherosclerosis. *J. Am. Coll. Cardiol.* 2007; 49:2073–2080. [PubMed: 17531655]

14. Lobatto ME, Fuster V, Fayad ZA, Mulder WJM. Perspectives and Opportunities for Nanomedicine in the Management of Atherosclerosis. *Nat. Rev. Drug Discovery*. 2011; 10:835–852.
15. O'Connor JPB, Jackson A, Parker GJM, Roberts C, Jayson GC. Dynamic Contrast-Enhanced MRI in Clinical Trials of Antivasular Therapies. *Nat. Rev. Clin. Oncol*. 2012; 9:167–177. [PubMed: 22330689]
16. Kerwin WS, Oikawa M, Yuan C, Jarvik GP, Hatsukami TS. MR Imaging of Adventitial Vasa Vasorum in Carotid Atherosclerosis. *Magn. Reson. Med*. 2008; 59:507–514. [PubMed: 18306402]
17. Fayad ZA, Fuster V, Fallon JT, Jayasundera T, Worthley SG, Helft G, Aguinaldo JG, Badimon JJ, Sharma SK. Noninvasive *In Vivo* Human Coronary Artery Lumen and Wall Imaging Using Black-Blood Magnetic Resonance Imaging. *Circulation*. 2000; 102:506–510. [PubMed: 10920061]
18. Calcagno C, Cornily J-C, Hyafil F, Rudd JHF, Briley-Saebo KC, Mani V, Goldschlager G, Machac J, Fuster V, Fayad ZA. Detection of Neovessels in Atherosclerotic Plaques of Rabbits Using Dynamic Contrast Enhanced MRI and 18F-FDG PET *Arterioscler. Thromb. Vasc. Biol*. 2008; 28:1311–1317.
19. Kim Y, Lobatto ME, Kawahara T, Lee Chung B, Mieszawska AJ, Sanchez-Gaytan BL, Fay F, Senders ML, Calcagno C, Becraft J, et al. Probing Nanoparticle Translocation across the Permeable Endothelium in Experimental Atherosclerosis. *Proc. Natl. Acad. Sci. U.S.A.* 2014; 111:1078–1083. [PubMed: 24395808]
20. Millon A, Boussel L, Brevet M, Mathevet J-L, Canet-Soulas E, Mory C, Scoazec J-Y, Douek P. Clinical and Histological Significance of Gadolinium Enhancement in Carotid Atherosclerotic Plaque. *Stroke*. 2012; 43:3023–3028. [PubMed: 22923447]
21. Phinikaridou A, Andia ME, Protti A, Indermuehle A, Shah A, Smith A, Warley A, Botnar RM. Noninvasive Magnetic Resonance Imaging Evaluation of Endothelial Permeability in Murine Atherosclerosis Using an Albumin-Binding Contrast Agent. *Circulation*. 2012; 126:707–719. [PubMed: 22753191]
22. Liu JTC, Mandella MJ, Crawford JM, Contag CH, Wang TD, Kino GS. Efficient Rejection of Scattered Light Enables Deep Optical Sectioning in Turbid Media with Low-Numerical-Aperture Optics in a Dual-Axis Confocal Architecture. *J. Biomed. Opt.* 2008; 13:034020. [PubMed: 18601565]
23. Liu JTC, Mandella MJ, Ra H, Wong LK, Solgaard O, Kino GS, Piyawattanametha W, Contag CH, Wang TD. Miniature Near-Infrared Dual-Axes Confocal Microscope Utilizing a Two-Dimensional Microelectromechanical Systems Scanner. *Opt. Lett.* 2007; 32:256–258. [PubMed: 17215937]
24. Ra H, Piyawattanametha W, Mandella MJ, Hsiung P-L, Hardy J, Wang TD, Contag CH, Kino GS, Solgaard O. Three-Dimensional *In Vivo* Imaging by a Handheld Dual-Axes Confocal Microscope. *Opt. Express*. 2008; 16:7224–7232. [PubMed: 18545427]
25. Liu JTC, Loewke NO, Mandella MJ, Leigh SY, Levenson RM, Crawford JM, Contag CH. Real-Time Pathology through *In Vivo Microscopy*. *Stud. Health Technol. Inf.* 2013; 185:235–264.
26. Liu JTC, Loewke NO, Mandella MJ, Levenson RM, Crawford JM, Contag CH. Point-of-Care Pathology with Miniature Microscopes. *Anal. Cell. Pathol.* 2011; 34:81–98.
27. Liu JTC, Mandella MJ, Loewke NO, Haeberle H, Ra H, Piyawattanametha W, Solgaard O, Kino GS, Contag CH. Micromirror-Scanned Dual-Axis Confocal Microscope Utilizing a Gradient-Index Relay Lens for Image Guidance during Brain Surgery. *J. Biomed. Opt.* 2010; 15:026029. [PubMed: 20459274]
28. Lobatto, ME.; Calcagno, C.; Metselaar, JM.; Storm, G.; Stroes, ESG.; Fayad, ZA.; Mulder, WJM. Imaging the Efficacy of Anti-Inflammatory Liposomes in a Rabbit Model of Atherosclerosis by Non-invasive Imaging. 1st ed.. Vol. 508. Amsterdam: Elsevier Inc; 2012. p. 211-228.
29. Fogel U, Ding Z, Hardung H, Jander S, Reichmann G, Jacoby C, Schubert R, Schrader J. *In Vivo* Monitoring of Inflammation after Cardiac and Cerebral Ischemia by Fluorine Magnetic Resonance Imaging. *Circulation*. 2008; 118:140–148. [PubMed: 18574049]
30. Moulton KS, Vakili K, Zurakowski D, Soliman M, Butterfield C, Sylvan E, Lo KM, Gillies S, Javaherian K, Folkman J. Inhibition of Plaque Neovascularization Reduces Macrophage Accumulation and Progression of Advanced Atherosclerosis. *Proc. Natl. Acad. Sci. USA*. 2003; 100:4736–4741. [PubMed: 12682294]

31. Parathath S, Mick SL, Feig JE, Joaquin V, Grauer L, Habel DM, Gassmann M, Gardner LB, Fisher EA. Hypoxia Is Present in Murine Atherosclerotic Plaques and Has Multiple Adverse Effects on Macrophage Lipid Metabolism. *Circ. Res.* 2011; 109:1141–1152. [PubMed: 21921268]
32. Cormode DP, Skajaa T, van Schooneveld MM, Koole R, Jarzyna P, Lobatto ME, Calcagno C, Barazza A, Gordon RE, Zanzonico P, et al. Nanocrystal Core High-Density Lipoproteins: A Multimodality Contrast Agent Platform. *Nano Lett.* 2008; 8:3715–3723. [PubMed: 18939808]
33. Hrkach J, Von Hoff D, Ali MM, Andrianova E, Auer J, Campbell T, De Witt D, Figa M, Figueiredo M, Horhota A, et al. Preclinical Development and Clinical Translation of a PSMA-Targeted Docetaxel Nanoparticle with a Differentiated Pharmacological Profile. *Sci. Transl. Med.* 2012; 4:128ra39.
34. Jarzyna PA, Skajaa T, Gianella A, Cormode DP, Samber DD, Dickson SD, Chen W, Griffioen AW, Fayad ZA, Mulder WJ. Iron Oxide Core Oil-in-Water Emulsions as a Multifunctional Nanoparticle Platform for Tumor Targeting and Imaging. *Biomaterials.* 2009; 30:6947–6954. [PubMed: 19783295]
35. Kirpotin DB, Drummond DC, Shao Y, Shalaby MR, Hong K, Nielsen UB, Marks JD, Benz CC, Park JW. Antibody Targeting of Long-Circulating Lipidic Nanoparticles Does Not Increase Tumor Localization but Does Increase Internalization in Animal Models. *Cancer Res.* 2006; 66:6732–6740. [PubMed: 16818648]
36. Cabral H, Matsumoto Y, Mizuno K, Chen Q, Murakami M, Kimura M, Terada Y, Kano MR, Miyazono K, Uesaka M, et al. Accumulation of Sub-100 nm Polymeric Micelles in Poorly Permeable Tumours Depends on Size. *Nat. Nanotechnol.* 2011; 6:815–823. [PubMed: 22020122]
37. Nel AE, Madler L, Velegol D, Xia T, Hoek EM, Somasundaran P, Klaessig F, Castranova V, Thompson M. Understanding Biophysicochemical Interactions at the Nano-Bio Interface. *Nat. Mater.* 2009; 8:543–557. [PubMed: 19525947]
38. Vinegoni C, Botnaru I, Aikawa E, Calfon MA, Iwamoto Y, Folco EJ, Ntziachristos V, Weissleder R, Libby P, Jaffer FA. Indocyanine Green Enables Near-Infrared Fluorescence Imaging of Lipid-Rich, Inflamed Atherosclerotic Plaques. *Sci. Transl. Med.* 2011; 3:84ra45.
39. Gu XI, Palacio-Mancheno PE, Leong DJ, Borisov YA, Williams E, Maldonado N, Laudier D, Majeska RJ, Schaffler MB, Sun HB, et al. High Resolution Micro Arthrography of Hard and Soft Tissues in a Murine Model. *Osteoarthritis Cartilage.* 2012; 20:1011–1019. [PubMed: 22613702]
40. Palacio-Mancheno PE, Larriera AI, Doty SB, Cardoso L, Fritton SP. 3D Assessment of Cortical Bone Porosity and Tissue Mineral Density Using High-Resolution  $\mu$ CT: Effects of Resolution and Threshold Method. *J. Bone Miner. Res.* 2014; 29:142–150. [PubMed: 23775635]



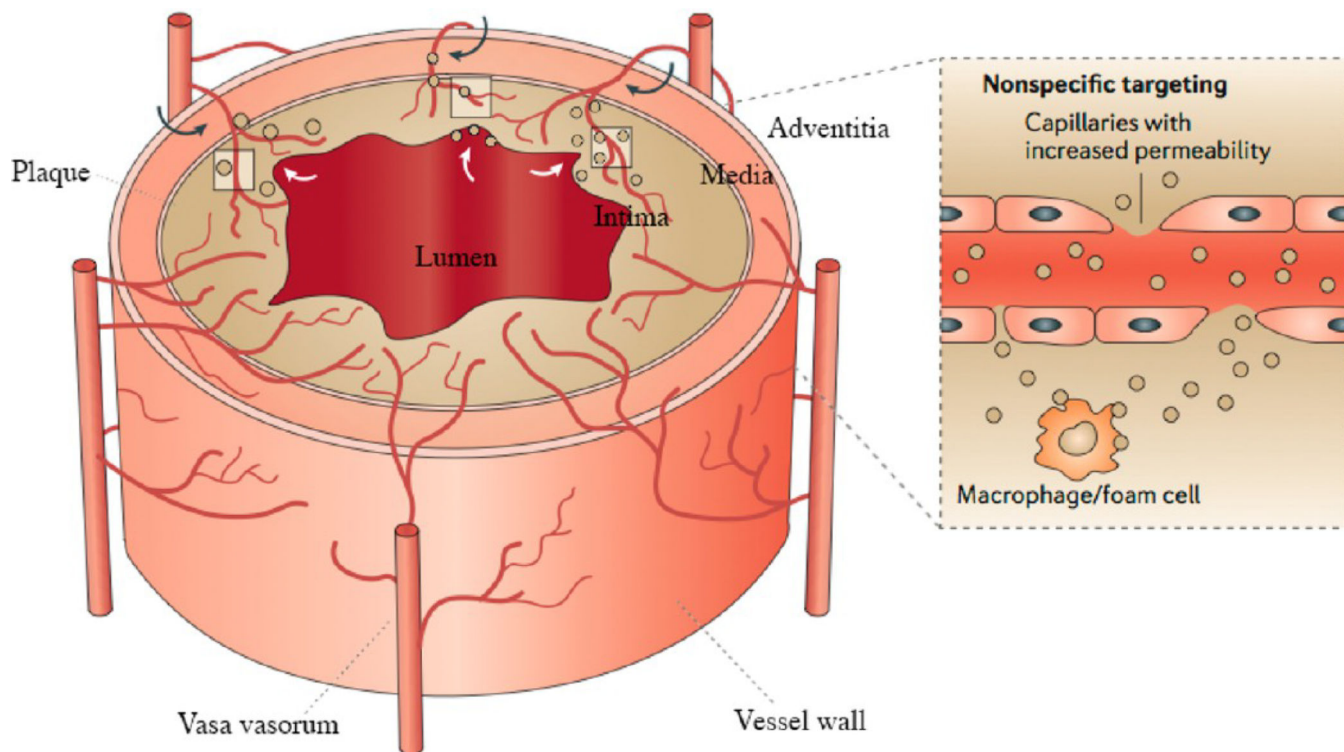


**Figure 1.** Schematic of mechanism of proposed nanoparticle targeting in atherosclerosis. The vasa vasorum surrounding the vessel wall of medium- and large-sized arteries expands and reaches into the plaque in advanced atherosclerosis due to hypoxia-induced angiogenesis. Long-circulating nanoparticles may accumulate in the plaque through the luminal side of the arterial vessel wall through the dysfunctional endothelial lining (intima), as well as through the dysfunctional neovessels that sprout from the adventitia (magnified) and are consequently phagocytized locally by macrophages. Adapted with permission from ref 14. Copyright 2011 Nature Publishing Group.

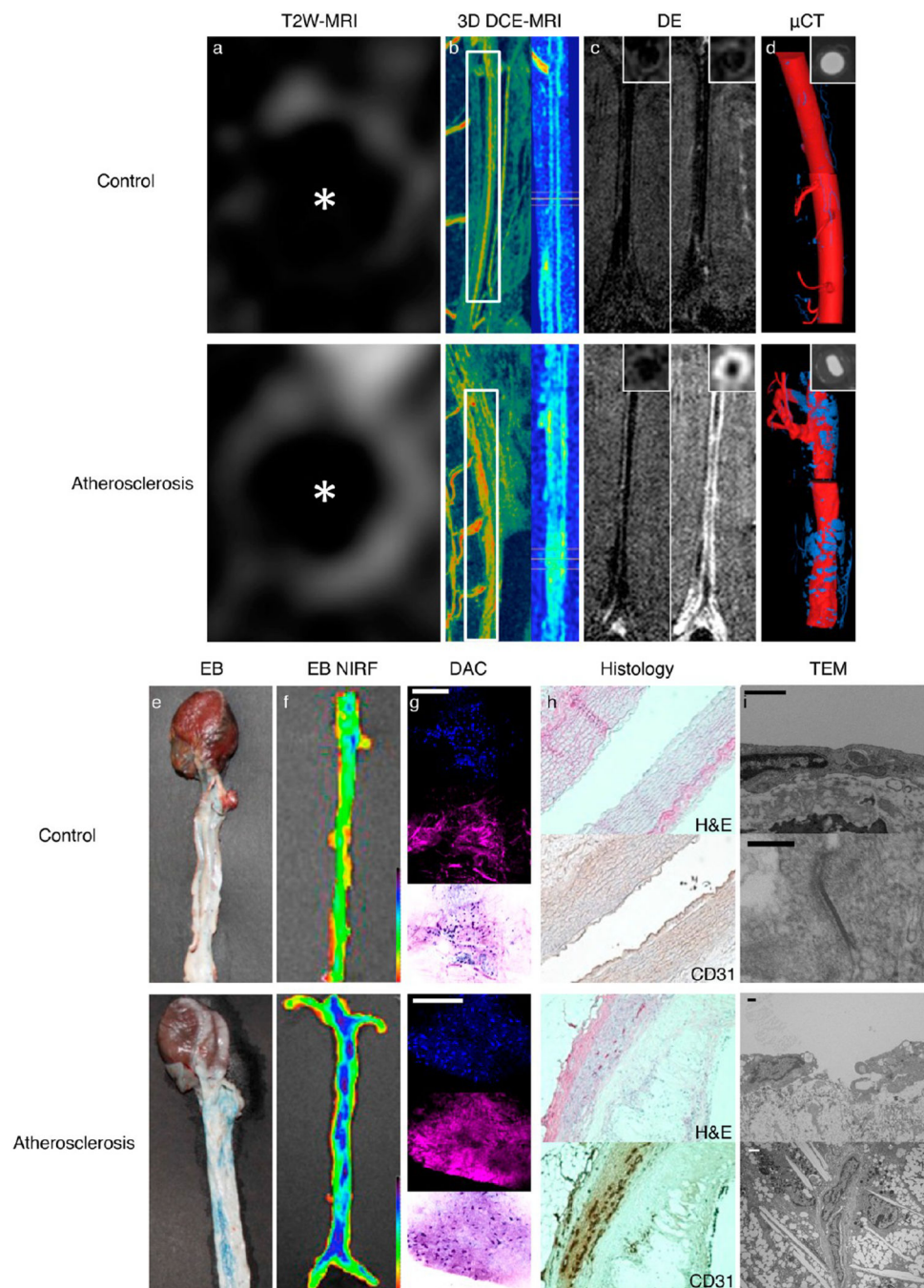


**Figure 2.** Comparison of *in vivo* and *ex vivo* imaging of control and atherosclerotic rabbits. (a) Conventional T2W-MRI shows a thickened arterial wall in rabbits with atherosclerosis; \*depicts lumen. (b) Sagittal 3D DCE-MRI images reveal a homogeneous vessel wall in healthy rabbits, while rabbits with atherosclerosis have several regions of permeability (red), also demonstrated in the adjoined reformatted images. (c) Coronal T1W delayed enhancement scans allow the quantification of contrast agent after 12 min. The vessel wall of atherosclerotic rabbits is markedly enhanced; the insets show the axial vessel walls pre-

and postcontrast. (d) Three-dimensional rendered  $\mu$ CT of aortas infused with a lead-based polymer reveal the abundant vasa vasorum (blue) surrounding the atherosclerotic vessel. The lumen is depicted in red. The insets show a single axial 6  $\mu$ m thick slice from which the 3D images were rendered. (e) Staining with Evans Blue dye (EB) demonstrates increased permeability of en face prepared thoracic aortas of atherosclerotic rabbits compared to healthy rabbits. (f) EB quantified with near-infrared fluorescence (NIRF) imaging revealed higher EB uptake in the abdominal aorta of atherosclerotic rabbits. (g) Dual-axis confocal microscopy (DAC) images display the intimal structure of a healthy and an atherosclerotic rabbit. The images are color coded for the appearance of an H&E stain. The top panel shows methylene blue staining—color coded blue to approximate hematoxylin, the middle panel indocyanine green—color coded pink to approximate eosin and the bottom panel is a color-mapped composite with an H&E appearance (scale bar 100  $\mu$ m). (h) Histological staining with hematoxylin and eosin and CD-31 for endothelial cells confirms *in vivo* findings of increased vessel wall thickness and increased microvasculature surrounding the vessel wall, as well as neovessels in the plaque. (i) Transmission electron microscopy (TEM) of the healthy and atherosclerotic vessel wall. Aligned endothelial cells are seen in the healthy vessel wall, with a tight junction magnified (scale bars 1 and 0.5  $\mu$ m). In the atherosclerotic vessel wall, large paracellular gaps are seen between endothelial cells; in addition, a neovessel in the plaque is shown (scale bars 2  $\mu$ m).

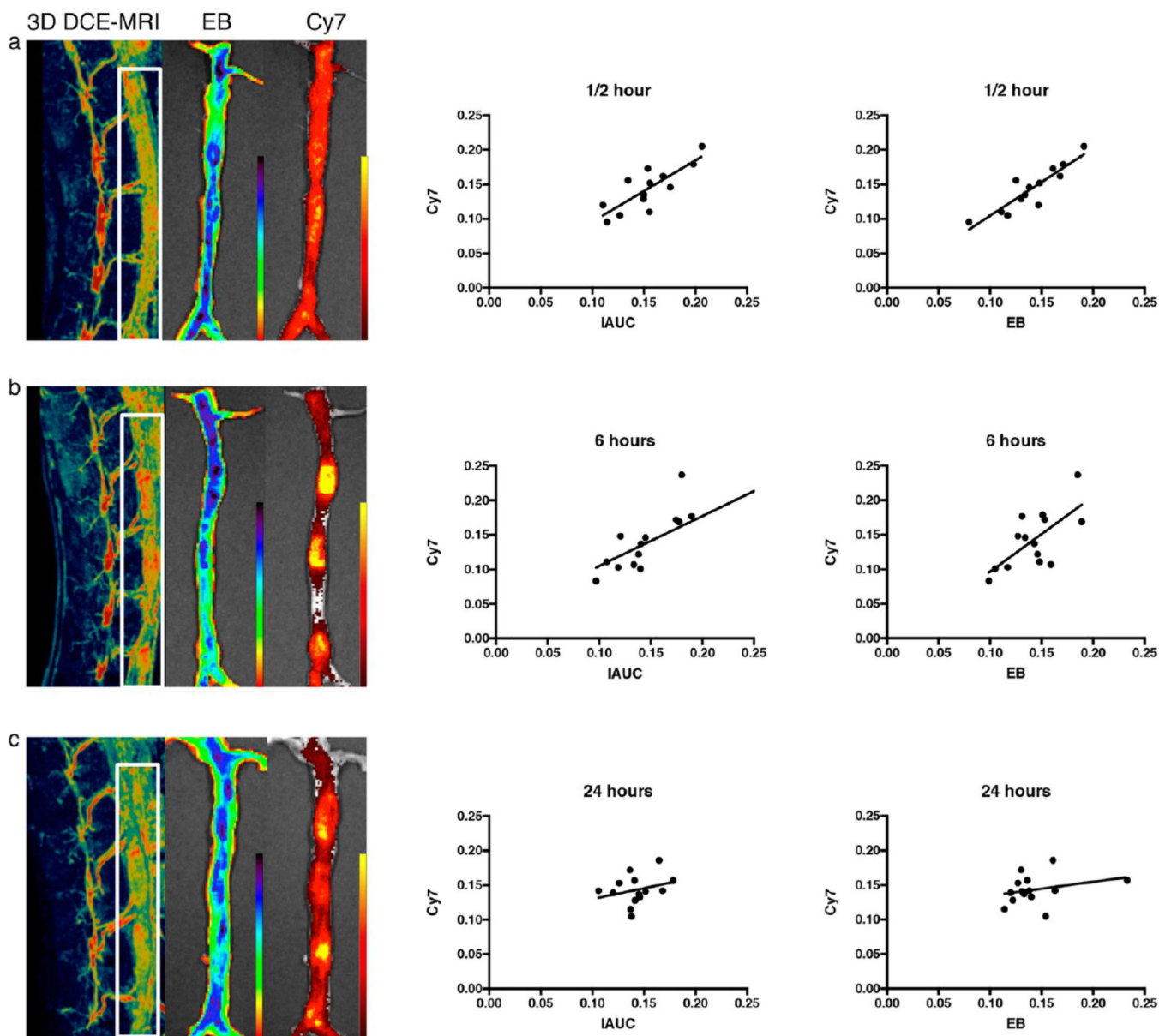


**Figure 3.** Correlation of *in vivo* 3D DCE-MRI, *ex vivo* EB, and Cy7-liposomal nanoparticle (Cy7-LN) optical imaging over time. Sagittal *in vivo* 3D DCE-MRI IAUC maps of abdominal aortas of rabbits with atherosclerosis, next to the matching *ex vivo* EB and Cy7-LN images, together with the resultant linear regression maps at different time points. Correlation of nanoparticle accumulation with *in vivo* and *ex vivo* imaging parameters is excellent after 30 min (a), decreases after 6 h (b), and has no relation after 24 h (c).



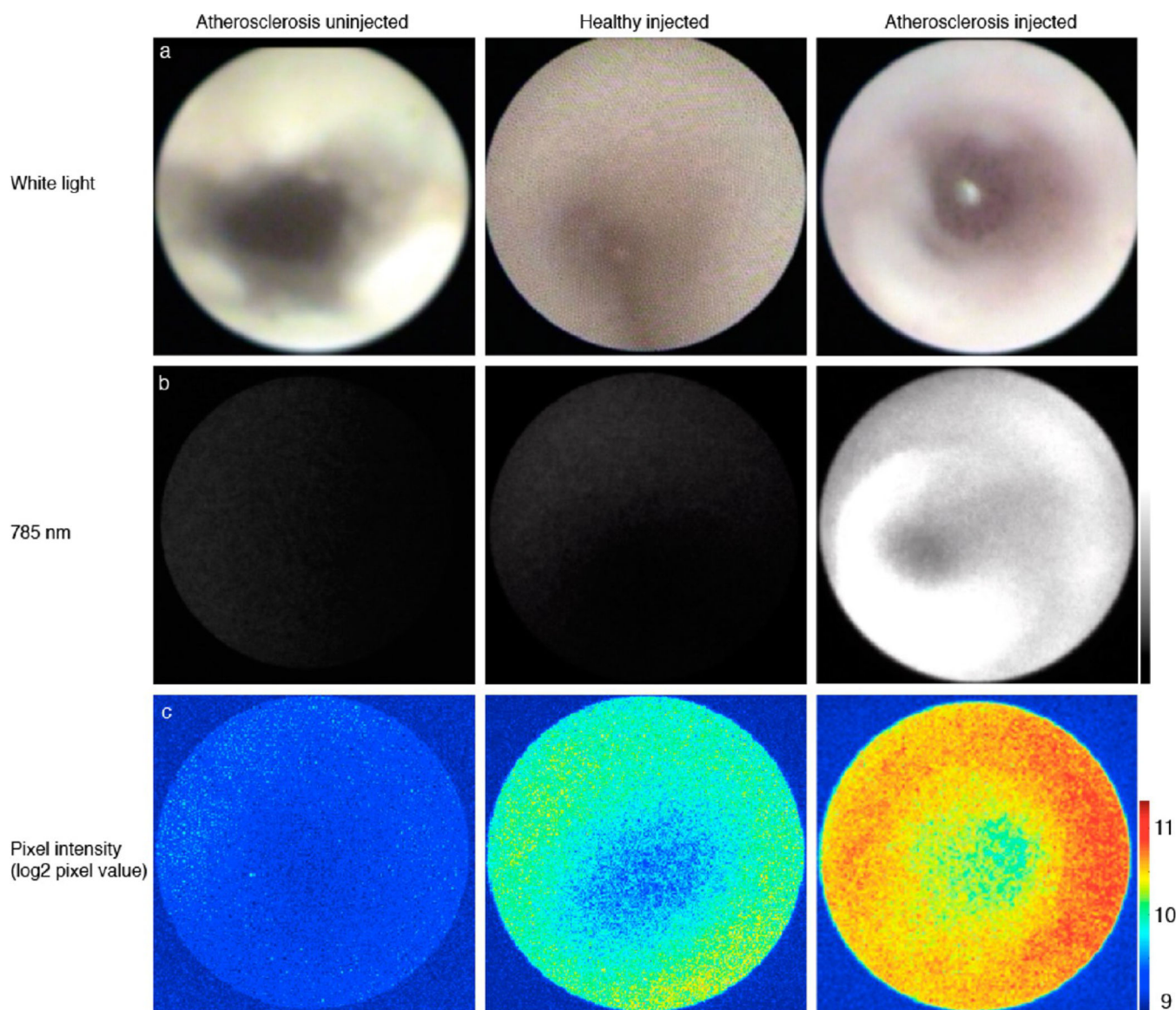


**Figure 4.** *Ex vivo* intravascular imaging of healthy and atherosclerotic aortas injected with liposomal nanoparticles imaged with a fluorescent and white light fiberscope using a 785 nm laser system. (a) White light imaging, (b) fluorescence imaging at 785 nm, and (c) pixel intensity mapping reveal pronounced nanoparticle uptake after 24 h in an atherosclerotic abdominal aorta injected with liposomal nanoparticles compared to control animals.

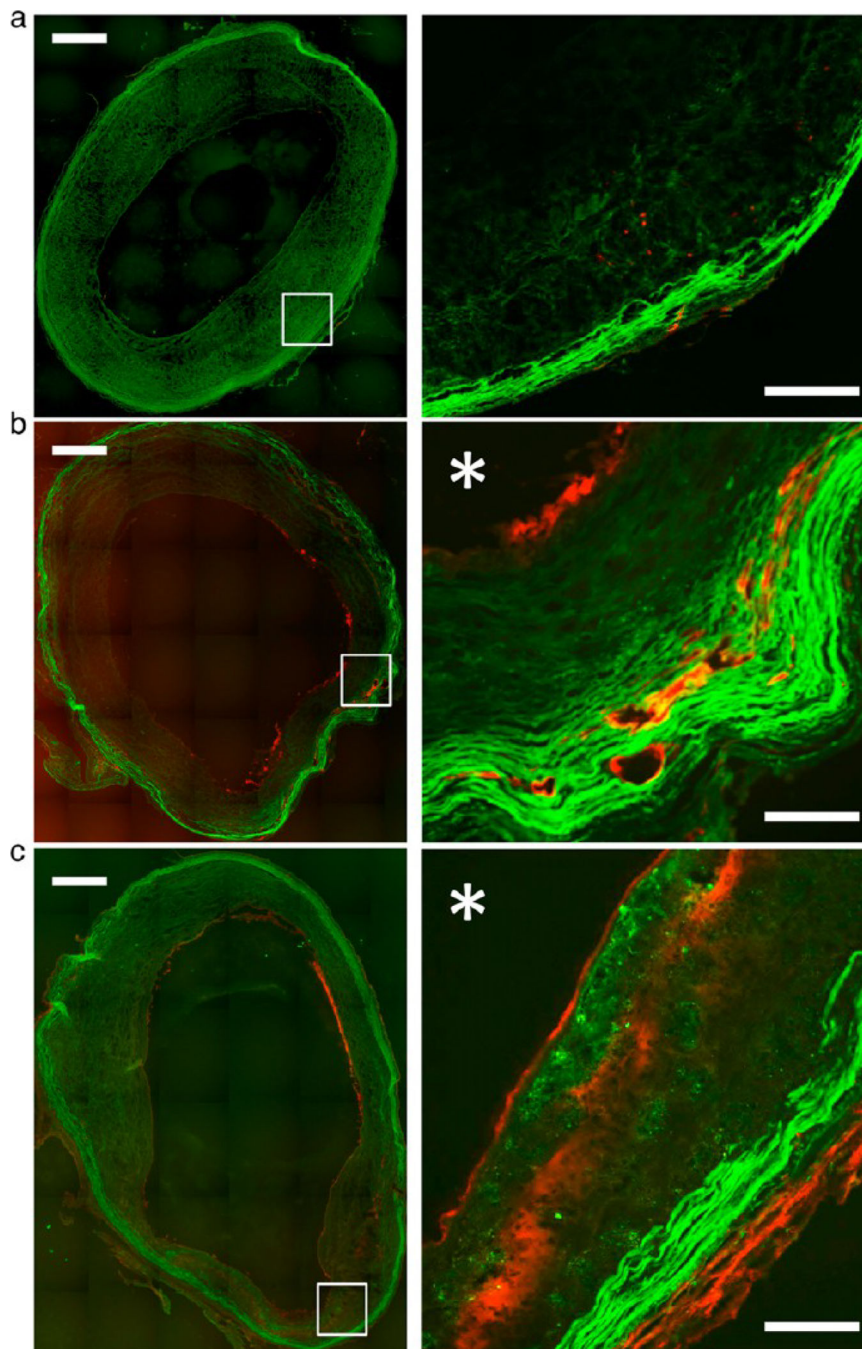


**Figure 5.** Fluorescence microscopy of nanoparticle accumulation in atherosclerotic lesions at different time points. (a) Stitched fluorescence microscopy of a 5  $\mu\text{m}$  thick aortic section of the rabbit sacrificed after 30 min (scale bar 500  $\mu\text{m}$ ). Cy5.5 liposomal nanoparticles (red, Cy5 channel) can be seen confined to the vasculature. The white square gives a view of the magnification on the right (scale bar 50  $\mu\text{m}$ ). (b) After 6 h, nanoparticles start to enter from the luminal side of the aorta as well as starting to extravasate from the vasa vasorum. (c) Twenty-four hours later, nanoparticles can be seen at the luminal side, the vasa vasorum, and dispersed



throughout the plaque. \*Indicates the lumen of the vessel. Red = Cy5.5-LN, green = FITC channel (autofluorescence). Alternative color scheme available as Supplementary Figure 6.

Author Manuscript

Author Manuscript

Author Manuscript

Author Manuscript

**TABLE 1**

Overview of Differences in Imaging Parameters in Rabbits Fed a Chow Diet *versus* Rabbits with Atherosclerosis

<b>modality</b>	<b>healthy (SD)</b>	<b>atherosclerosis (SD)</b>	<b>P value</b>
T2W-MRI (MWA, mm <sup>2</sup> )	0.09 (0.02)	0.13 (0.05)	<0.0001
3D DCE-MRI (IAUC)	1.43 (0.11)	3.79 (0.38)	<0.0001
Delayed enhancement (%)	34.8 (42.1)	177.8 (84.3)	<0.0001
EB (area %)	2.78 (2.3)	12.05 (6.3)	=0.033
EBNIRF ( $\times 10^{11}$ )	1.62 ( $1.63 \times 10^{10}$ )	2.81 ( $8.2 \times 10^{10}$ )	=0.02

Author Manuscript

Author Manuscript

Author Manuscript

Author Manuscript